Experimental Analysis of the Thermal Energy Storage Potential of a Phase Change Material embedded in Additively Manufactured Lattice Structures

Stefano Piacquadio[1,c], Maximilian Schirp-Schoenen[1], Mauro Mameli[2], Sauro Filippeschi[2], Kai-Uwe Schröder[1]

1 RWTH Aachen University, Institute for structural mechanics and lightweight design, Wüllnerstraße 7, 52062, Aachen, Germany
2 University of Pisa, Department of Energy, Systems, TErritory and Constructions Engineering (DESTEC), Largo Lucio Lazzarino 1, Pisa, Italy

c: corresponding author
Email: stefano.piacquadio@sla.rwth-aachen.de

Abstract

Recent literature introduced novel additively manufactured porous metallic structures designed to deliver enhancement of the thermal conductivity of organic phase change materials. Among these, so-called lattice structures are of particular interest for application in lightweight components. Originally investigated for their attractive mass-specific mechanical properties, these geometries were recently proposed, in alternative to metallic foams, as a conductive matrix of phase change materials. However, the geometrical parameters of a lattice structure differ from the ones of a metallic foam and no established data exist in the literature about the influence of the lattice cell geometry on the transient heat transfer enhancement of a phase change material. This work presents an experimental comparison of the thermal behaviour of a composite based on an n-Octadecane paraffin wax embedded in four different aluminium lattices with varying unit cell topology ($f_2$ccz, bcc, bccz, $f_2$bcc), but showing the same cell size, aspect ratio and strut diameter. It is noticed that the unit cell topology affects the transient thermal behaviour beyond its direct effect on the cell porosity. To address this, a specific thermal performance parameter is identified. The sample based on the $f_2$ccz topology represents the best candidate. The influence of orientation with respect to gravity on the heat transfer is also investigated. While the samples show relatively low porosity, ranging from 70.7% to 83.4%, the wide pore diameters lead to a high impact of melt convection on the thermal behaviour of most samples. Up to 28% wall temperature variation is evidenced for different heating orientations.

Keywords:
Phase Change Material; Additive Manufacturing; Lattice Structures; Metamaterial; Multifunctional structure

Nomenclature

MFS: Multifunctional Structure
AM: Additive Manufacturing
LPBF: Laser Powder Bed Fusion
PCM: Phase Change Material
PPI: Pores Per Inch
BCC: Body Centered Cubic
FCC: Face centered cubic
IR: Infrared
PWM: Pulse Width Modulation
STP: Specific Thermal Performance

Symbols

ϕ : Porosity
ξ : Volume fraction

1. Introduction

Multifunctional Structures (MFSs) [1] are structural concepts aiming at an holistic mass reduction of systems where mass and volume saving are the major design driver, e.g. in aerospace or automotive systems. In order to perform relevant mass reduction, the MFSs often embed envelopes or cases hosting specific devices: payloads, electronic boards, batteries, instruments and controlling devices. The thermal control systems must therefore interact with the MFS or be even embedded into the MFS itself. At the moment, there is a growing interest in the analysis of composite material that can pursue different tasks: a good thermal control performance, a high mechanical stress resistance and a low weight. Fredi et al. [2],[3] recently investigated thermal and mechanical properties of fibre-reinforced composites embedding microencapsulated paraffin-based Phase Change Materials (PCMs). This way, components capable to couple a thermal energy storage functionality, or thermal damping one, with a mechanical load-carrying capability were introduced. As most PCMs for low to medium temperature application (0 °C to 100 °C) exhibit a low thermal conductivity, several methods to improve the thermal performance of PCMs are proposed in the literature, as summarised in [4]. Rehman et al. in [5] presented a wide review of the open literature on the use of macroencapsulated PCM, with conductive matrices made of open celled metal or carbon foams. They show that the use of open cell metallic foams is an effective way to increase the thermal conductivity of the PCM up to 20-30 times. The most investigated metallic structure is based on a foam made of metallic Kelvin cell, characterised by the relative density and the pore size (PPI number). The sizes and the cells morphologies affect the thermal performances by decreasing the PCM melting time. Usually, the main heat transfer mode inside the composite material is conduction. However, recent works observed that the effect of melt natural convection on the thermal performance is not negligible. This phenomenon can be significant in hypergravity environment [6], [7] and in the case of foams with low PPI [8]–[10].
Recently, the use of Additive Manufacturing (AM) technologies for metallic alloys allowed considering a wider range of periodic metallic matrix geometries for such purpose. As explained by Rehme [11], a wide variety of unit cell topologies, inspired by the cubic Bravais crystal lattice types, can be manufactured via Laser Powder Bed Fusion (LPBF). As shown in Figure 1, in addition to face centered cubic (fcc or $f_2$cc) and body centered cubic ones (bcc), the so-called $f_2$bcc cells obtained by a combination of the previous two can be manufactured. With vertically oriented (z) struts, so-called bccz and $f_2$ccz unit cells can be obtained. The geometry of these lattice cells is characterised by their cell size, strut diameter, aspect ratio and unit cell topology. The volume fraction is then a function of these independent variables. In contrast, foams are characterised only by their volume fraction and the number of pores per inch (PPI). These might be of interest for a MFS application. Indeed, the mechanical behaviour of cellular solids based on periodic truss lattices is related to higher mechanical properties at the same relative density with respect to foams [12]–[19].

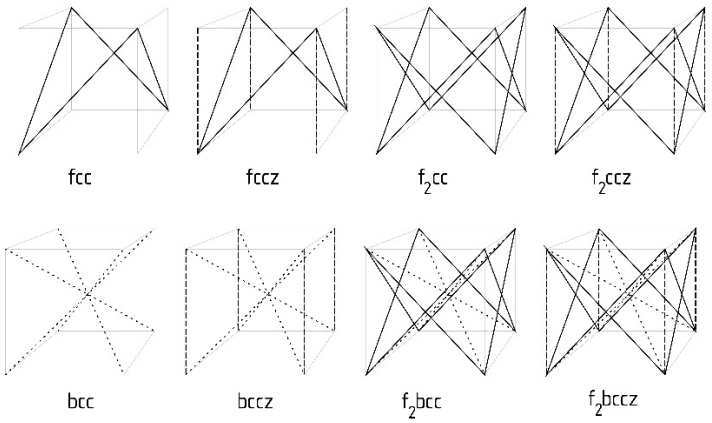

Figure 1: Schematic representation of the different cubic truss-lattice unit cell topologies

Some authors investigated the thermal performance of composites embedding different PCMs, based on paraffin waxes, within such lattice structures. Zhang et al. in [20] proposed a lattice core sandwich

structure made of additively manufactured aluminium alloy (AlSi10Mg) which was embedded with a paraffin wax. The matrix was based on the bcc unit cell and was also functionally graded through variation of the strut diameter. The test sample included external walls which were added integrally to the structure in the additive manufacturing process to avoid liquid PCM leakage. They investigated the thermal performance both numerically and experimentally and observed that full melting time decreases up to a rate of 20% in case of grading of the structure. Similarly, Righetti et al. in [21] investigated the heat transfer performance of four different PCM composite samples based on aluminium lattice structures with bcc unit cell topology. Each sample had the same porosity, but different unit cell sizes and strut diameters. They noticed that the sample with the smallest cell size delivered the best thermal performance, reducing the melting time by 17% with respect to the absence of lattices. Dudon et al. in [22] tested and compared two similar PCM modules for satellite applications. One was embedded with an additively manufactured lattice core structure also based on the bcc unit cell. The other one embedded additively manufactured fins. They found that the module based on a lattice structure had a better thermal performance. While the use of additively manufactured lattice structures seems to deliver promising performance enhancement for a PCM, limited information is available on the effect of the various geometrical parameters of such matrices on the overall thermal performance. As discussed, previous works included combined variations of the strut diameter and of the unit cell size. To the authors' knowledge, only the recent work of Hubert et al. [23] proposed an analysis of different lattice unit cell topologies for PCM thermal performance enhancement. They developed and validated a semi-analytical model to evaluate the effective thermal conductivity of four different cell types, namely, according to the presented nomenclature, bcc, $f_2$cc, bccz and $f_2$ccz. Their model showed that such cell types can show up to 75% higher effective thermal conductivity with respect to open-celled foams at the same relative density. They also indicated that such lattice cells have an orthotropic thermal conductivity. However, the experimental investigations that were carried out this far to analyse the behaviour of lattice cells embedded into a PCM material are scarce. No information is available on the transient thermal performance of the composite material with different unit cell topologies. In addition, there are several open issues that must be investigated. Especially, it is not clear whether the effective thermal conductivity is the only factor determining the thermal performance of different unit cells at the same porosity. To the authors' knowledge, no information is available regarding the influence of orientation on the expansion of the melting front in such structures.

This work aims at experimentally investigating on the thermal performance enhancement potential of composite samples with different unit cell topologies, under different gravity orientations. The tests are performed using four samples with different unit cell topologies, namely bcc, bccz, $f_2$ccz and $f_2$bcc. All samples have the same aspect ratio, cell size and strut diameter. Each sample is tested heating in three different orientations, respectively with heat flux vector in the same direction of the local gravity vector, orthogonal to it and with opposite direction. The qualitative effect of the natural convection regime occurring inside the cells is detected. The thermal control performance of the cells is measured in order to obtain the best multifunctional performance, or else the highest thermal performance with the lowest mass. In order to improve the comparability between the thermal performance of samples and other metallic/PCM structures, a dimensionless term indicating the specific thermal performance characteristic is introduced.

2. Experimental setup

The experimental setup, schematically described in Figure 2, consists of the composite specimens, the heating system, the containment box, the measurement instruments and the data acquisition system. All the specimens used in the experiment were additively manufactured by EOS GmbH, using an AlSi10Mg aluminium alloy. They have a cubic shape with an edge length of 50 mm. The internal structure is periodically filled by a single unit cell. The samples have unit cells with the same cell width of 5 mm, strut diameters of 1 mm and a cubic shape. Due to the different amount and geometrical configuration of the struts of each different cell, the volume fraction is not the same among the tested samples. This is calculated and reported in Table 1. The provided samples allow one to determine the effect of unit cell topology on the heat transfer, while maintaining cell size, aspect ratio and strut diameter constant. Two sides of the cube are closed with two 1 mm thick sheets which are additively manufactured with

the samples. The other four sides are left open to allow observation of the phase change phenomenon and integration of temperature sensors. The samples are shown in Figure 3.

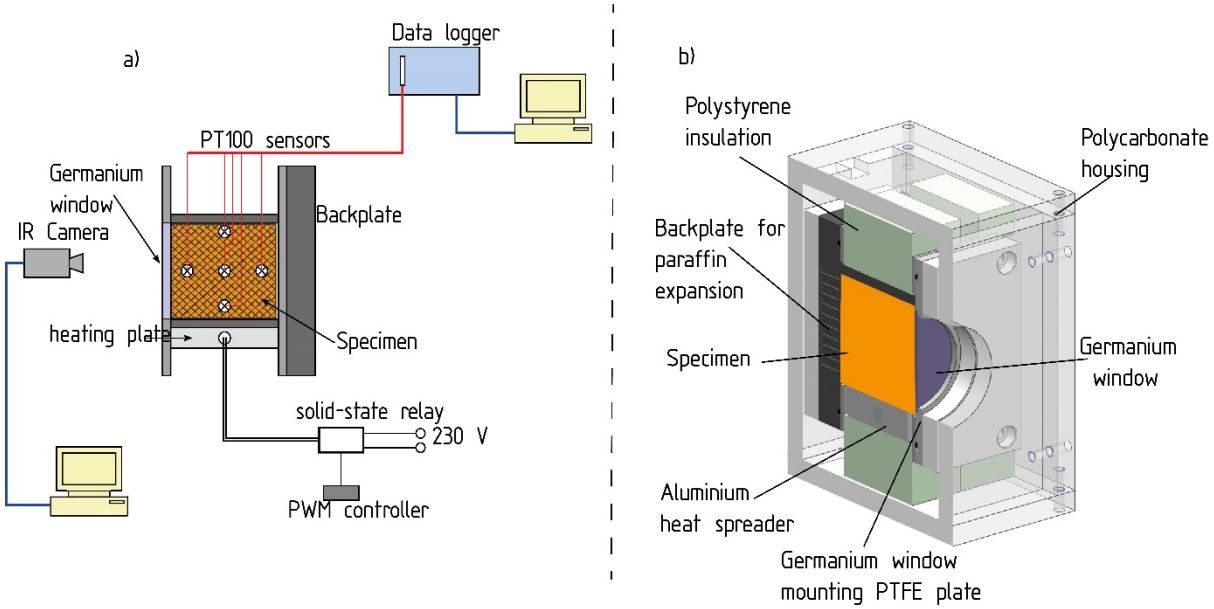

Figure 2: a) schematic view of the experimental setup, b) CAD section view of the test cell highlighting enclosures

Table 1: Summary of volume fraction and porosity of the different cell types calculated through the dedicated CAD software

Cell type	Solid volume fraction χ [vol %]	Porosity ϕ [vol%]	Strut diameter [mm]	Cell width P_s [mm]	Aspect ratio
$f_2$ccz	16.6	83.4	1	5	1:1:1
bcc	17.8	82.2	1	5	1:1:1
bccz	20	80	1	5	1:1:1
$f_2$bcc	29.3	70.7	1	5	1:1:1

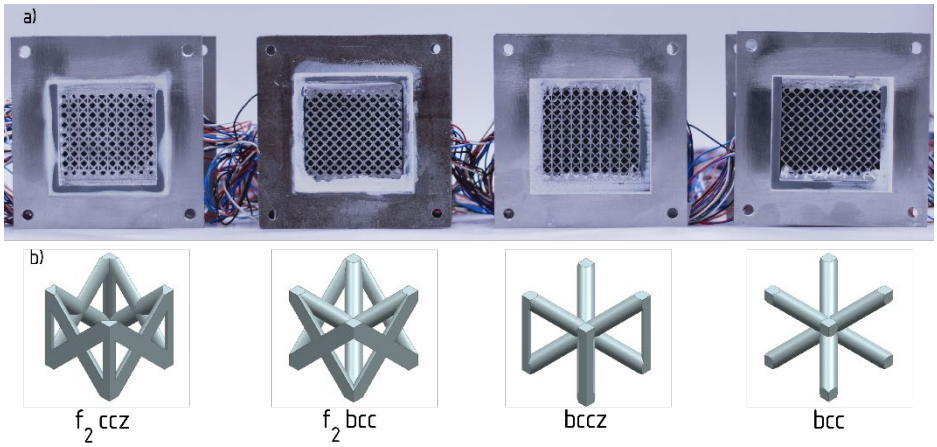

Figure 3:a) view of the specimens with window mount flanges, b) correspondent unit cell topology

The heating systems consists of a cartridge heater having length of 50 mm and diameter of 6.5 mm (100 W class from Horst GmbH, Germany). The cartridge heater is fitted into an aluminium heat spreader with dimensions 15 mm x 50 mm x 50 mm. A PWM controller with a solid-state relay (CL240D05 by Crydom Inc., USA) is used to keep the input power constantly at 40 W. A high conductivity paste is used to ensure a proper thermal contact between the aluminium face sheet of the test sample and the

heat spreader. As shown on the left-hand side of Figure 2a, a Germanium window is mounted on a flange and sealed on the test sample surface to allow Infrared (IR) visualization of the melting front expansion under different orientations. On the opposite side an expansion plate, so-called backplate (Figure 4a), is mounted. This contains 100 empty chambers with 1 mm wide square holes. Such holes have the role of allowing a homogeneous PCM volume expansion of up to 10% during the melting and mitigate the risks related to pressure build-up. The component is additively manufactured out of a plastic material (proprietary resin from Formlabs, Inc) and bolted to one side of the cubic specimen. An O-ring offers an airtight sealing. The measurement system consists of temperature sensors and IR visualisation. Ten four-wire PT100 temperature sensors are symmetrically placed on two of the lateral sides of the cube, as shown in Figure 4b. They have an accuracy of $\pm$0.21 K at 40 °C (tolerance class F 0,15 A by Heraeus GmbH, Germany). The sensors are labeled according to their proximity to the heating plate and further based on the two instrumented sides "A" and "B", as shown in Figure 4b) and Figure 5. "A-heat" and "B-heat" are therefore the sensors closest to the heating plate, "A-mid" and "B-mid" the ones placed at the middle of the additively manufactured cube and "A-end", "B-end" are the farthest sensors from the heat spreader. The PT100 sensors are connected via a PXI interface to a data logger (NI PXIe-1078 by National Instruments Corporation®). The commercial software Dasylab® (by measX GmbH) is used to process and store the acquired data. The sensors envelope is bonded using a bi-component epoxy glue on three of the six surfaces of the cubic specimen to obtain an airtight PCM container. This infrared inspection is done using a medium wave cooled IR camera (ImageIR® 8300 from Infratec GmbH).
The whole test cell is enclosed in a Polycarbonate box together with polystyrene foam (Styrodur®) isolating the test cell from environment, as shown in Figure 2b). The PCM material chosen to is the n-Octadecane paraffin wax (purity of 99%, produced by abcr GmbH, Germany), characterised by a melting point of 29 °C. The thermal properties of the PCM are shown in Table 2.

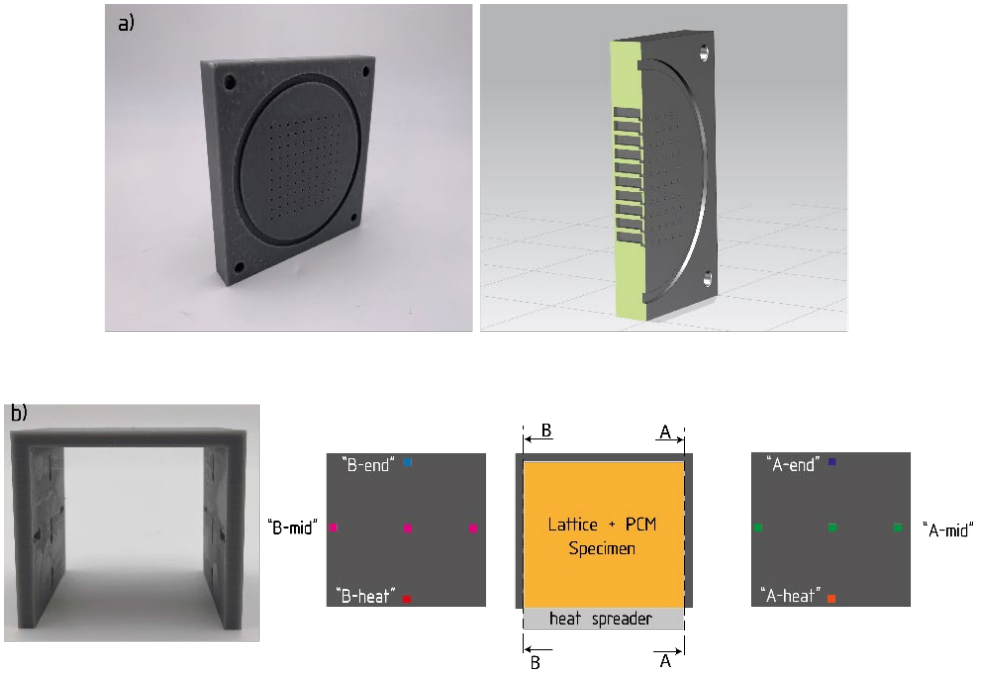

Figure 4: a) CAD and as manufactured image of the backplate for PCM volume expansion pressure relieve, b) envelope hosting slits for allocation of temperature sensors as schematically shown. Red and orange dots denote "B-" and "A-heat" sensors, light- and dark-blue denote "B-" and "A-end" sensors, magenta and green denote "B-" and "A-mid" sensors

Table 2: Thermophysical properties of the employed n-Octadecane paraffin wax, supplied by abcr GmbH, Germany.

Property	n-Octadecane (solid)	n-Octadecane (liquid)

Density	814 kg/m^3	774 kg/m^3
Specific heat capacity	2150 J/kgK	2180 J/kgK
Thermal conductivity	0.358 W/mK	0.152 W/mK
Melting point	29 °C	-
Heat of fusion	244 kJ/kg	-

2.1 Experimental test campaign

All the tests have been performed by keeping constant the heat flux, providing a constant heat power of 40 W to it. The tests are repeated with different orientations with respect to the gravity in order to detect the role of the convective heat transfer inside the samples. Three different orientations of the heat flux vector with respect to gravity are considered, as schematically shown in Figure 5. The orientation of the sample is defined by the mutual orientation of the heat flux vector and the gravitational acceleration, $\vec{g}$. Every cell is tested at each orientation three times to assess the repeatability. As shown in Figure 5, the orientations denominated top and bottom are referred to the case with the heat flux parallel to gravity and the same or opposite directions, respectively. At the side orientation the heat flux vector is orthogonal to $\vec{g}$. It is important to notice that the inclination variation is applied rotating both the heat source and the test sample together. This means that the samples which present z-struts ($f_2$ccz and bccz) are always heated in a direction parallel to these, independently of the orientation. The test sample is filled with the paraffin wax and cooled down to 18°C within a climate chamber (Espec® ARS-1100) in order to achieve a common initial temperature for each sample and each run. The tests are carried out by heating and observing the sample during the melting phenomenon. The IR images and the temperature data are acquired during all the melting period with a sampling rate of 5 Hz. The tests are interrupted as the paraffin wax is totally molten or as a sensors "A-heat" or "B-heat" achieves a temperature of 60 °C. This procedure is done to prevent overheating of the Styrodur® insulation, which starts to decompose above 80 °C.

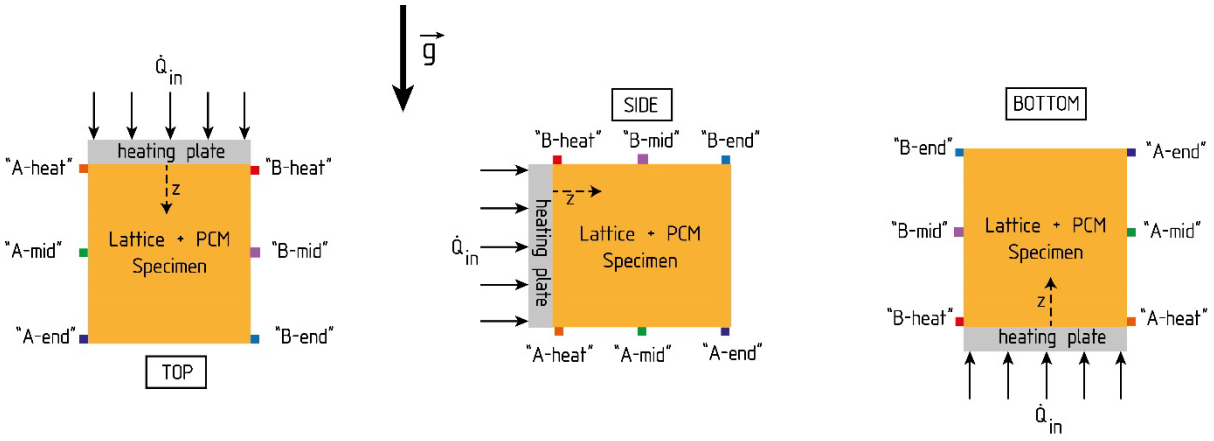

Figure 5:Schematic view of the test orientations employed for each test sample and the relative position of the PT100 sensor rows with respect to the input heat flux.

3. Experimental results

The thermal performance analysis of each sample is performed by comparing temperature evolutions during the melting process. The reference sample is the $f_2$ccz because it presents the lowest thermal conductivity along the plane orthogonal to the heat flux direction, while the heat conduction in z direction should be promoted. The temperature evolution of the sensors for the $f_2$ccz sample are shown in Figures 6-8. For sake of clearness, the temperatures plotted in the figures at the three different spatial locations ("heat", "mid" and "end") are averaged between the available sensors at such location. The shaded areas of the same colour of the sensor line represent the standard deviation relative to the repeatability tests. The melting point is identified in the figures by a black horizontal line at the corresponding temperature. The evolution of the temperatures of the rest of the samples are similarly plotted and annexed in Appendix B. The relevant results, i.e. the comparison among the thermal performances of different samples are described in the following section.

Figure 6, Figure 7 and Figure 8 show the test results for, respectively, the top, the side and the bottom heating orientation of the $f_2$ccz sample. All the figures show a similar trend. At time zero, as heat is supplied, all the temperatures begin to grow up with different slopes in relation to their proximity at the heating surface (solid material). As the temperature approaches the melting point, it remains nearly constant for a short time to then begin increasing again with a different slope (liquid).

Different behaviours can be distinguished for the different orientations as soon as the temperatures reach the melting point. In particular, when heating at side orientation (Figure 7) the temperature trends of the "A-mid" and "B-mid" sensors, as well as the "A-end" and "B-end" sensors show different slopes with respect to what shown in the plots relative to top and bottom orientations (Figure 6, Figure 8). This indicates a spatially inhomogeneous expansion of the melting front, due to a convection regime insurgence. Figure 7, shows that the standard deviation of the "B" side sensors tends to increase after the melting point. This also can be attributed to the occurring of convective motions in the molten liquid. The average maximum temperature obtained for the test at top heating configuration is 60.8 °C after 900 s. At the same experiment time, 54.6 °C is the average maximum temperature for the side orientation tests, while 54.3 °C for the bottom ones. The best and the worst performance as thermal control device has been observed in the case of bottom and top orientation, respectively. The IR image acquisition allows a preliminary detection of the natural convective regime occurrence. This tendency is evaluated for each gravity orientation. IR frames at different time points for each orientation of each tested unit cell can be found in Appendix A.

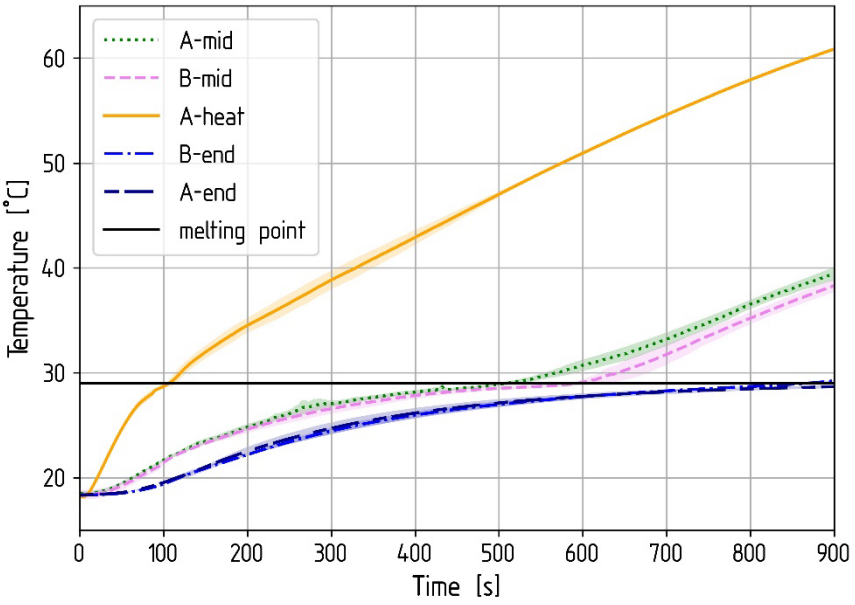

Figure 6:Results of the $f_2$ccz cell type experiments for the top configuration.

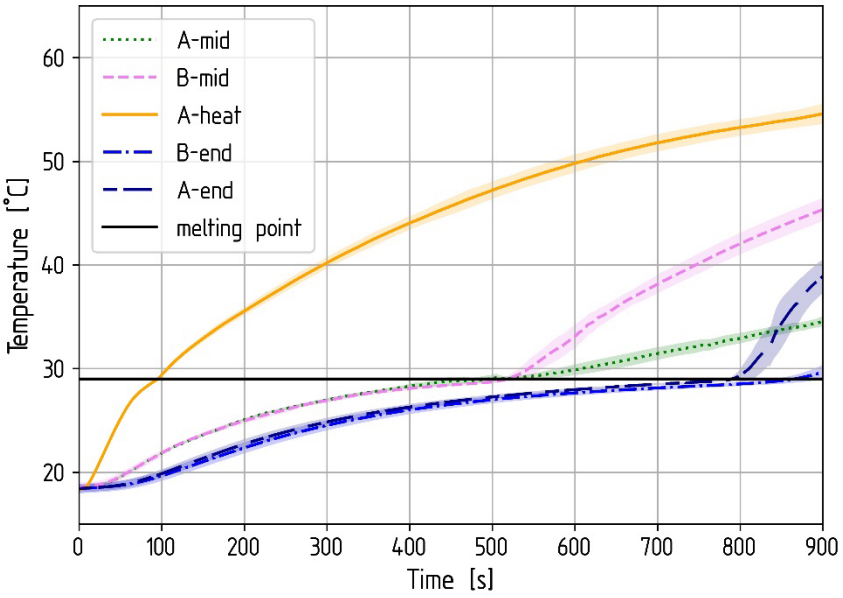

Figure 7:Results of the f2ccz cell type experiments for the side configuration.

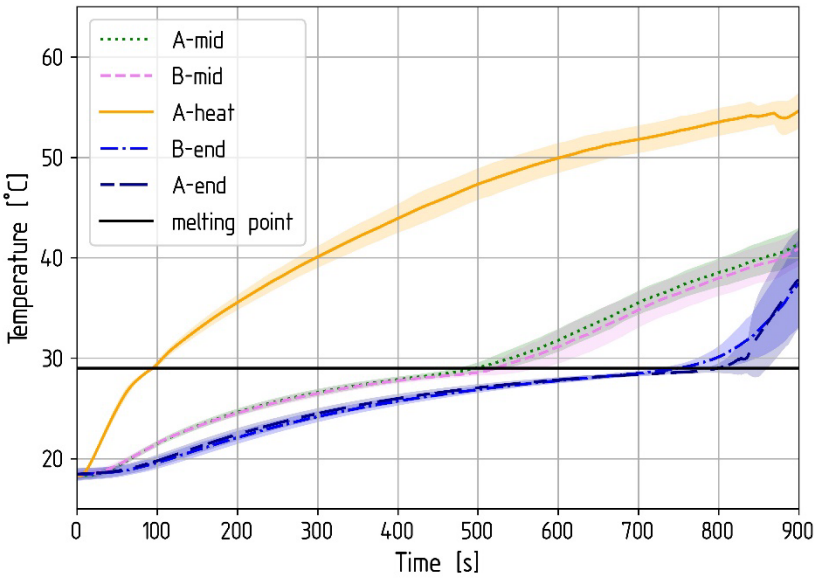

Figure 8:Results of the f2ccz cell type experiments for the bottom configuration.

3.1 Comparison of thermal performance for different samples

As previously shown, the thermal performance of each sample are well characterized by the temperature at the heating surface. The lower is the wall overheating with respect to the melting temperature measured at the heating surface the higher is the thermal performance of the sample as a thermal control device.

Another important temperature trend is relative to the sensors placed at “mid” location. The time at which such sensors reach the melting point is linked to the melting time of the samples.

To compare the performances of different samples the temperature trends of the "A-heat" and "A-mid" sensors are plotted over time for each tested sample at different orientations in Figure 9, Figure 10 and Figure 11. These indicate the comparisons of results under top, side and bottom orientation, respectively. In particular, the comparison is performed until the time point at which the sensors "A-mid" of all samples have reached the melting point, it corresponds to 635 s, exactly as the test sample with the bcc unit cell starts to melt at "mid" location. Figure 9 shows that the lowest temperature increase of the wall temperature (A-heat sensor) is obtained by the $f_2$bcc cell during the top-orientation tests. Here the natural convection inside the sample can be considered marginal. The growing slopes of the wall temperature over time are mainly affected by the thermal conductivity along the z axis (Table 3).

The sample based on the $f_2$ccz cell topology shows the second lowest temperature increment of the heating wall, followed by bccz and bcc cell types. The wall overheating in the case of $f_2$bcc is 65% lower than the worst case (bcc). A 31.2% difference between the maximum reported temperature of the $f_2$ccz and bcc samples is evidenced. However, as the two samples porosities differ only by 1.2%, this indicates a dominant role of the cell topology in influencing the heat transfer in the sample. Figure 10 and Figure 11 show a similar qualitative trend. The sample with the best performance is still the $f_2$bcc one, which shows the highest thermal conductivity along the z-axis. On the other hand, the growing slopes of the temperature trends are lower than the top orientation. This is due to the convection insurgence that enhances the heat transfer inside the composite. It can be noticed that bccz and $f_2$ccz samples show a closer temperature evolution. Especially bcc and bccz samples substantially vary their thermal performance when heating is imposed from the side and bottom orientations. This is analysed in detail in the following section.

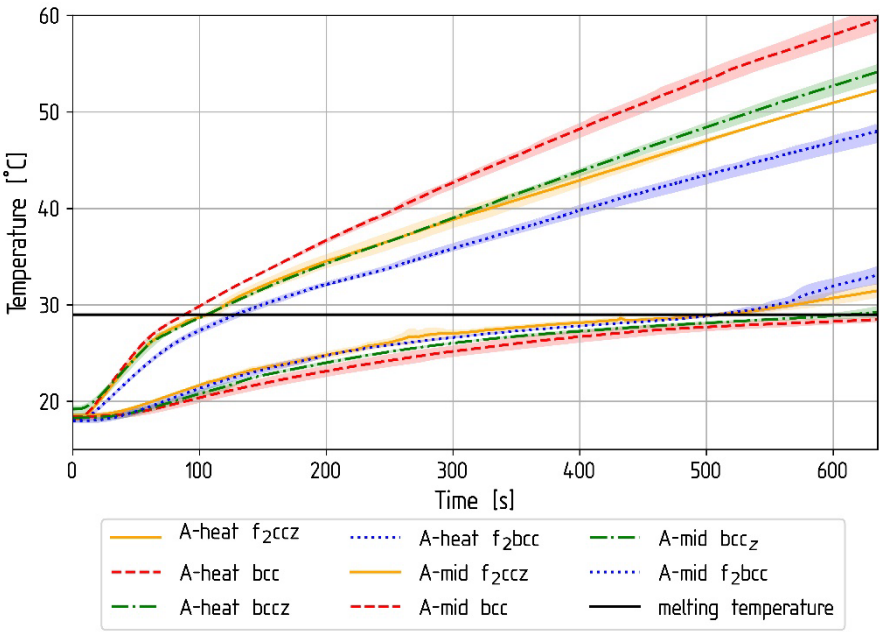

Figure 9: Comparison of the results for the four different cell types tested at the top orientation. Information is reported respectively for the A-heat and A-mid sensor rows

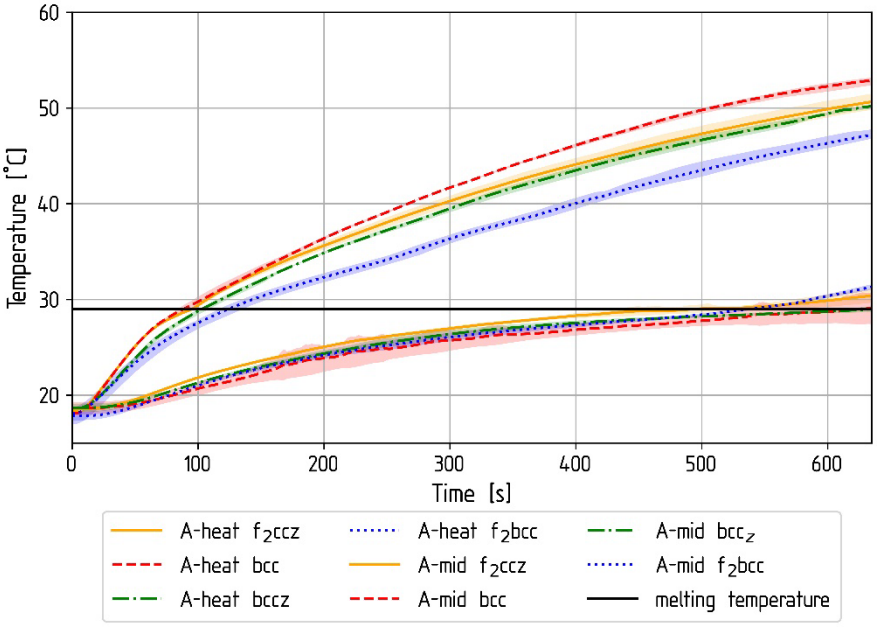

Figure 10:Comparison of the results for the four different cell types tested at the side orientation. Information is reported respectively for the A-heat and A-mid sensor rows

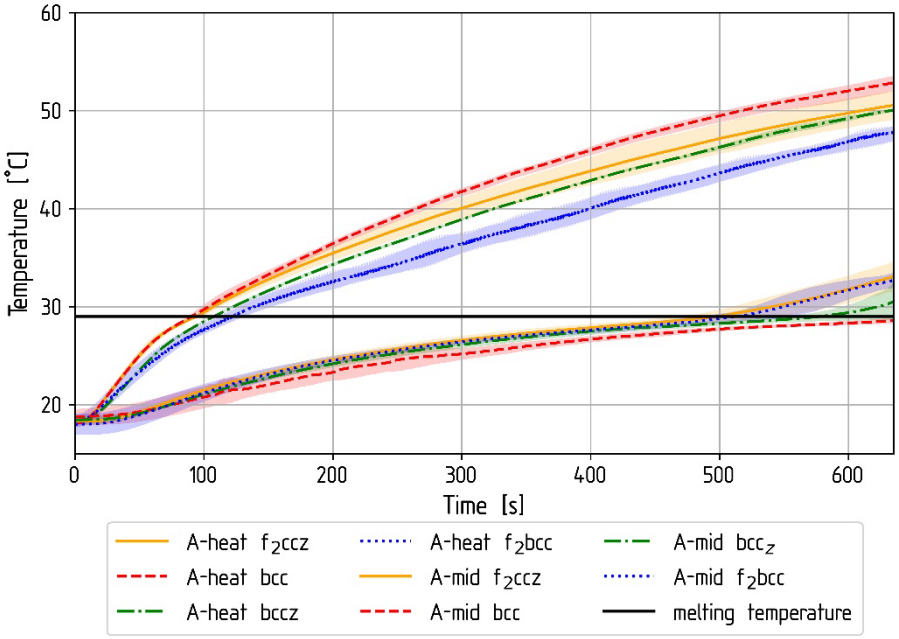

Figure 11:Comparison of the results for the four different cell types tested at the bottom orientation. Information is reported respectively for the A-heat and A-mid sensor rows

4. Overall performance assessment

In order to assess the performances of the samples as a multifunctional structure, an assessment criterion must be defined. The cell topologies of the tested samples have been chosen to match a good thermal performance with good mechanical behaviours and a low mass.

To compare the experimental results for the different samples and heating orientations, a non-dimensional criterion to assess the thermal performance has been defined based on the approach proposed by Diani and Campanale [24] for metal foams, and implemented also by Righetti et al. [21]

for lattice structures. First the wall overheating temperature, corresponding to the temperature of the "A-heat" sensor, is normalised as follows:

$$\theta = \frac{T_{A-heat} - T_{melt}}{T_{melt} - T_i} \quad (1)$$

where Θ is the non-dimensional wall overheating temperature, T_i the sample initial temperature, T_{melt} the paraffin wax melting temperature and lastly, T_{A-heat} is the temperature of the A-heat sensor, corresponding to the heated wall temperature. The Fourier and Stefan numbers are then used to quantify the transient heat conduction and the amount of latent heat absorption during the experiment. To define these, the effective diffusivity of the composite is calculated. The effective thermal conductivity of each sample is estimated with help of the model proposed by Hubert et al. [23]. The model is valid for cubic cells, i.e. size aspect ratio 1:1:1, and represents the sum of the contributions to the effective thermal conductivity given by the PCM and the one given by the solid material, over the control volume of a unit cell. The total heat power transferred through the control volume, Q_{tot}, can be separated in two terms, Q_{PCM} and Q_{solid}. These represent, respectively, the heat conducted through the PCM in the control volume and the heat along the struts of the solid material.

$$Q_{tot} = Q_{PCM} + Q_{solid} \quad (2)$$

Under the hypothesis of high porosity ϕ (i.e. high volume amount occupied by the PCM), the PCM cross section is considered constant. Thus, the first term on the right hand of Equation (2) is related to the cell porosity only. Due to the complex geometry, the term related to the solid material is obtained integrating a differential form of the Fourier's law:

$$Q_{solid} = \lambda_{solid}\, \Delta T / \int_0^{P_s} \frac{1}{A_s(s)} ds \quad (3)$$

where λ_{solid} is the solid bulk thermal conductivity, ΔT is the temperature gradient across the control volume, P_s is the width of the cubic cell and $A_s(s)$ is the cross-sectional area dependent on the strut longitudinal coordinate s. After some manipulation, the effective thermal conductivity of the unit cell in a given direction *i* (in-plane or out-of-plane), $\lambda_{eff,i}$, is written as:

$$\lambda_{eff,i} = \lambda_{PCM}\, \phi + \lambda_s G_{s,i}(1 - \phi) \quad (4)$$

where λ_{PCM} is the bulk thermal conductivity of the PCM, ϕ is the cell porosity, and $G_{s,i}$ is the direction dependent term that considers the complexity of the cross-section of the solid phase. For each cell the $G_{s,i}$ terms are obtained by Hubert et al. [23] as a function of the struts and nodes sizes and the effect of their interfaces. Applying the model and adapting it for the $f_2$bcc cell topology delivers the results reported in Table 3.

Table 3: Estimated effective thermal conductivities of the different samples in the out of plane and in-plane directions

Cell type	λ_{eff_z} $[W/mK]$	λ_{eff_xy} $[W/mK]$
$f_2$ccz	13.8	6.8
bcc	9.9	9.9
bccz	13.2	10.5
$f_2$bcc	19.1	14.1

The porosity ϕ (i.e. amount of volume occupied by the PCM) and the solid volume fraction χ are related by:

$$\phi = 1 - \chi \tag{5}$$

Thus, the effective density and specific heat capacity can be simply calculated through the mixture rule as follows:

$$\rho_{eff} = \phi \cdot \rho_{PCM} + \chi \cdot \rho_{solid} \tag{6}$$

$$Cp_{eff} = \phi \cdot \frac{\rho_{PCM}}{\rho_{eff}} \cdot Cp_{PCM} + \chi \cdot \frac{\rho_{solid}}{\rho_{eff}} \cdot Cp_{solid} \tag{7}$$

where ρ_{PCM} and Cp_{PCM} are the density and the specific heat capacity of the phase change material respectively, ρ_{solid} and Cp_{solid} are the bulk density and the specific heat capacity of the solid matrix. Similarly, the effective latent heat is defined as:

$$h_{eff} = \phi \cdot \frac{\rho_{PCM}}{\rho_{eff}} \cdot h_{PCM} \tag{8}$$

where h_{PCM} is the latent heat of the phase change material. With the so-obtained parameters, the Fourier number is defined as:

$$Fo = \frac{\lambda_{eff} \cdot t^*}{\rho_{eff} \cdot Cp_{eff} \cdot L^2} \tag{9}$$

where λ_{eff} is the effective thermal conductivity of the sample along the z axis, t^* is the characteristic time and L is the edge length of the sample. The Fourier number is calculated at the time t=635 s. This is the time at which the "mid" sensor for the bcc sample, heated at "top" heating orientation, reaches the PCM melting point. It represents the longest time to reach such temperature. The same sensors for both other samples at any orientation and the same sample at other orientations cross this threshold at lower experiment times.
The corrected Stefan number is defined considering the subcooling due to the initial temperature lower than the melting point, as suggested by Groulx and Lacroix [25]:

$$Ste' = \frac{Cp_{eff}(T_{A-heat} - T_{melt})}{h_{eff} + Cp_{eff}(T_{melt} - T_i)} \tag{10}$$

These non-dimensional parameters are calculated for each sample and each orientation and reported in Figure 12, where the non-dimensional temperature is plotted against the product of the Stefan and Fourier numbers. For sake of clarity, the results are compared with the correlation proposed by Diani and Campanale [24] for metallic foams:

$$\Theta = 1.9073(SteFo)^{(-0.717)} \tag{11}$$

Also the one proposed by Righetti et al. [21] for lattice structures is reported for comparison:

$$\Theta = 0.31(SteFo)^{(-0.69)} \tag{12}$$

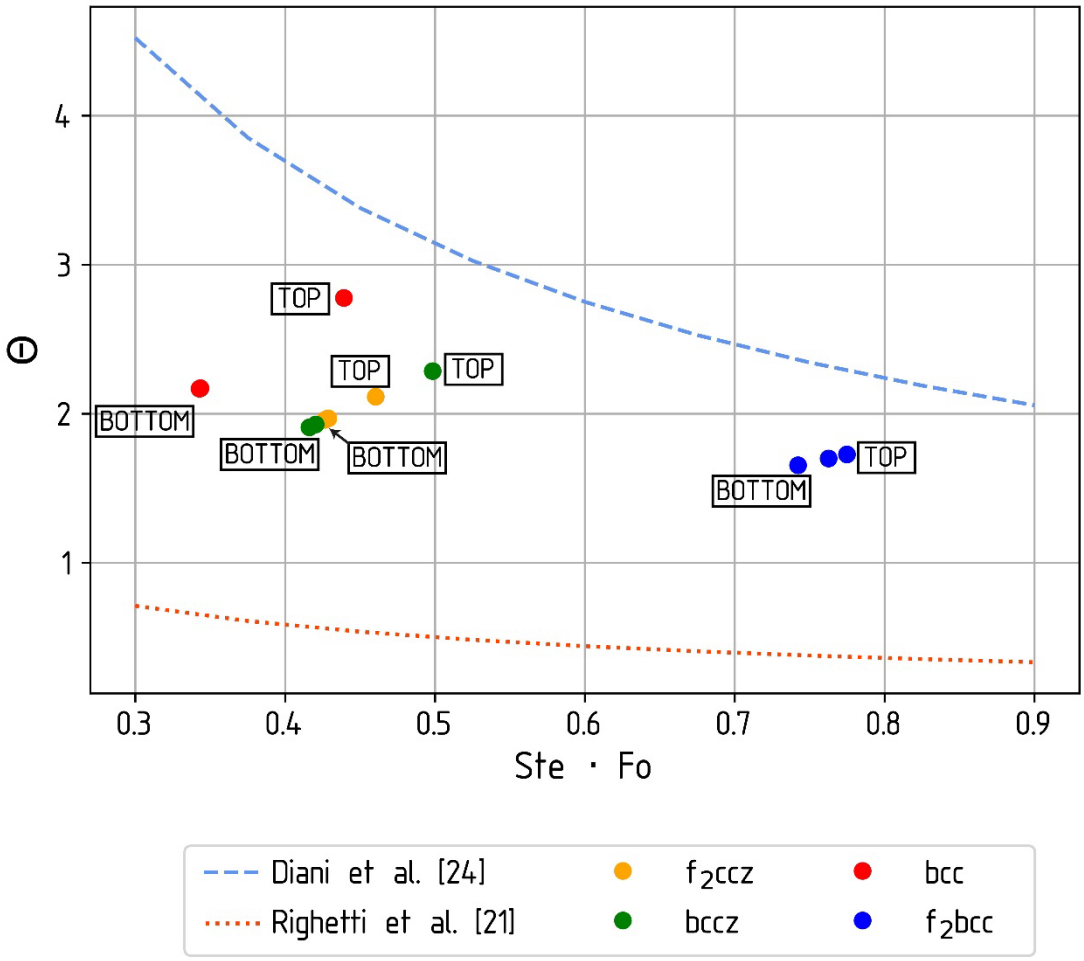

Figure 12: Dimensionless wall temperature against the product of the Stefan and Fourier numbers

Considering the results for the top heating orientation, it can be noticed that a good qualitative agreement is obtained with the model proposed by Hubert et al. [23]. However, Figure 12 shows that the heat transfer phenomenon is not dominated by conduction. Indeed, the side and bottom orientations show a non-dimensional temperature lower than the top orientation. A 28% reduction of the dimensionless temperature is noticed for the bcc sample between the top and the bottom orientations. Similar trends are noticed for all the topologies even if with lower reduction: 21% for the bccz sample, 8% for the $f_2$ccz one and 3% for the $f_2$bcc. Therefore, the convective effects cannot be neglected when considering the heat transfer performance of PCMs embedded in such lattice structures.

Diani and Campanale [24] and Righetti et al. [21] proposed power law correlations to describe the dependence of the wall overheating temperature on the product of the Stefan and Fourier numbers and thus on the geometry of the porous matrix. These are also reported in Figure 12. However, it is evident that a clear fit between the present data considering different heating orientations is not achievable.

In order to be able to compare the results obtained from such lattice cells with the data relative to foams, it is useful to relate the geometry of the tested lattice structures to the geometry of a metal foam. The parameter of the foam that mainly affects the convection insurgence is the PPI. Unfortunately, as previously stated, lattice structures geometrical parameters do not intrinsically include the definition of number of PPI to determine the geometry univocally. Therefore, the cells geometries are analysed with the commercial software nTopology®. The diameters of pores enclosed within the tested samples are mapped and calculated. The pore diameter is defined as the diameter of the largest sphere that fits inside a pore without overlapping the solid structure. However, the pores can overlap themselves. The calculation uses the graph representation of the lattice structures, which is made up of the centrelines of the individual struts. Thus, the calculated pore diameters do not depend on the strut diameters, but only on the cell size and its topology. Figure 13 shows the lattice structure (gray) and the spherical pores (pink) included within it. The equivalent pore diameter is calculated through a weighted average of the

resulting mapped pores. This way, a so-called equivalent PPI can be obtained for each cell. These are indicated in Table 5.

Table 4: Equivalent pores per inch for each tested sample, in order of decreasing porosity

Cell type	PPI_{eq}
$f_2$ccz	5
bcc	8
bccz	8
$f_2$bcc	20

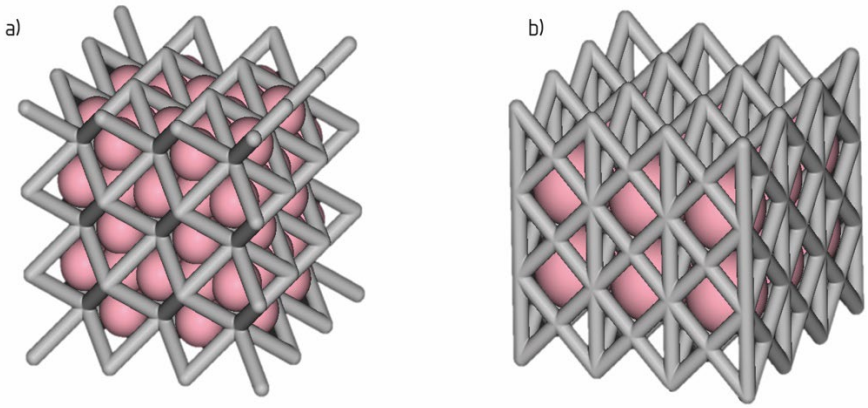

Figure 13: a) pores of the bcc sample, b) pores of the f2ccz sample

It can be noticed that the obtained data for the $f_2$ccz, bcc and bccz cells could be compared with metal foams characterised by low values of PPI. Several authors investigated the effect of the PPI on the thermal performance of metal foams/PCM composites, i.e. [6]–[10]. Their results show that lower numbers of PPI at the same foam porosity deliver lower wall temperatures and shorter melting times. The same qualitative behaviour is verified for the tested lattice structures. Unfortunately, lattice cells are not exactly a foam. It is possible to have cells topologies with the same equivalent PPI, but a different thermal behaviour. The orthotropic structure of the cell sample based on the bccz cell, which shows the same equivalent PPI of the bbc one, exhibits a lower wall temperature reduction with respect to the latter. Similar observations can be made regarding the $f_2$ccz sample, which shows the lowest PPI. This can be attributed to a combination of two factors: the conductive and convective contributions to the thermal behaviour of the composite are not independent, and the permeability of the structure is not directly correlated to the number of pores. Especially, most cells exhibit orthotropic topologies, which also might lead to direction dependent permeabilities. Furthermore, the effect of the thermal conductivity along the orthogonal plane cannot be neglected. It affects the melting front dynamic shape and the thermal performances too. In case of bottom orientation, where the convective effect should be lower than the side orientation, the transversal thermal conductivity can play a relevant role in the heat transfer. Therefore, in order to predict the behaviour of the lattice cells structure, convection cannot be neglected at all.

To properly address the overall performance of the different cells topologies with the goal of obtaining a multifunctional structure, the effect of the different cells porosity (or volume fraction) shall be taken into account. As described above, the highest specific thermal performance is not trivially connected to the thermal conductivity of the different cells topologies at the same porosity. Therefore, a more general assessment criterion must be defined. The thermal performance is directly related to modified Stefan number. A low wall temperature increase is wished, in order to obtain good thermal performance. The modified Stefan number is hereafter considered to be a relevant measure of the thermal energy storage

potential of a composite material at the same porosity. A Stefan number which tends to zero means that it is possible to store large amount of latent heat energy with no temperature overheating along the heating walls. Figure 14 shows the Stefan number against the volume fraction of the respective unit cell topologies. It can be stated that the highest overall performance is obtained by the sample which, at a given heating orientation, shows the lowest Stefan number and the lowest volume fraction, i.e. the highest the Stefan number relative to the previously discussed results is reported against the porosity of the respective unit cell topologies. As showcased by the $f_2$bcc unit cell, the lowest wall temperature increase is not directly related with the lowest Stefan number. It can be stated that the highest specific thermal performance is obtained by the sample which, at a given heating orientation, shows the lowest possible Stefan number and the lowest possible volume fraction.

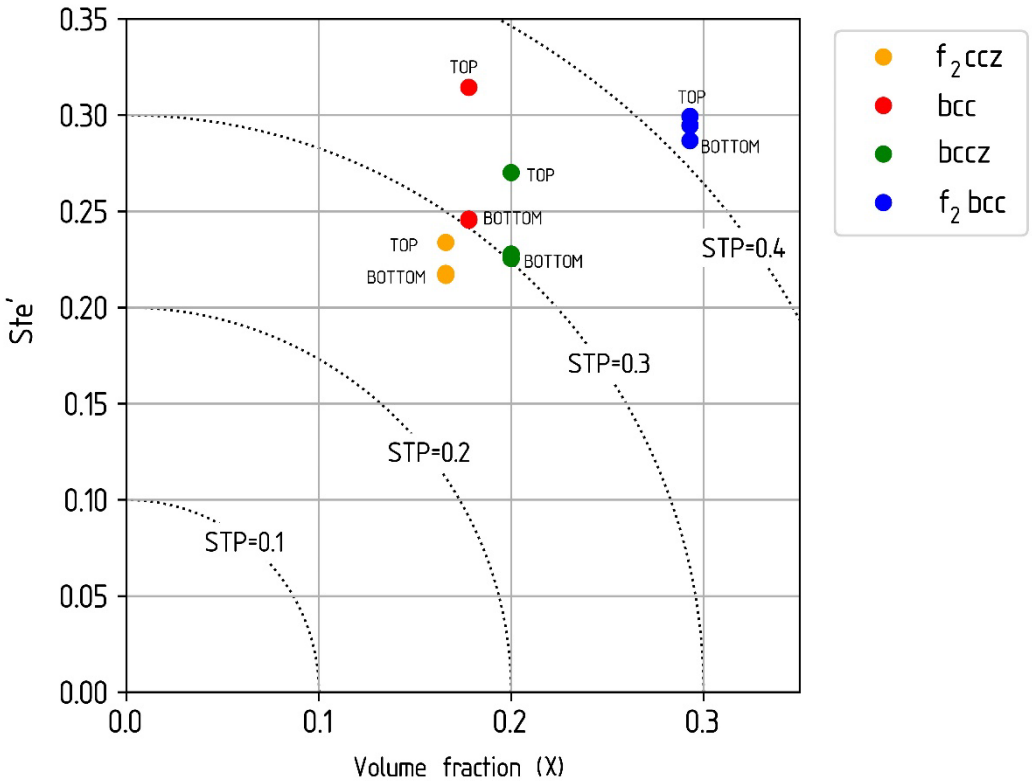

Figure 14: Comparison of the different obtained Stefan numbers for each test at each heating orientation, against the volume fraction of the respective samples. Dashed isolines corresponding to the same specific thermal performance are reported

To quantitatively estimate the overall thermal performance, the distance of each point from the origin of the plot reported in Figure 14 can be considered, as indicated in equation (8). This way, the thermal performance and the mass have the same importance in the overall performance definition.

$$STP = \sqrt{Ste'^2 + \chi^2} \tag{13}$$

where STP is the specific thermal performance, Ste the Stefan number and χ the volume fraction of the unit cell. The STP data points are reported in Table 4.

Table 5: Specific Thermal Performance data points for each unit cell topology and each heating orientation

Unit cell	Top	Side	Bottom
f₂ccz	0.28	0.27	0.27
bcc	0.36	0.30	0.30
bccz	0.33	0.30	0.30

$f_2$bcc	0.42	0.41	0.41

Clearly, the lowest values of the STP parameter indicate the best specific thermal performance. From this it can be noticed that, while in absolute terms the $f_2$bcc sample delivers the lowest wall temperature increase, this is mainly due to the low porosity of the sample. If one considers using such a composite material in automotive or aerospace applications, where the mass of the device has similar importance to the thermal performance, it is relevant to indicate that actually, the $f_2$ccz sample shows the highest specific thermal performance for all heating orientations.

5. Conclusions

This work deals with an experimental analysis of additively manufactured lattice structures are tested as porous matrices of a paraffin wax phase change material. This composite material can be used as thermal control system for multifunctional applications where the weight of the structure assumes a relevant role. In particular, the effect of the unit cell topology on the heat transfer enhancement of the phase change material is experimentally investigated. Four different specimens are realised and tested. The lattice structure samples have the same cell size, strut diameter and aspect ratio, but different unit cell topology. The four topologies are namely $f_2$bcc, bccz, bcc and $f_2$ccz. Additionally, the samples are tested under three different orientations in order to investigate the effect of inclination with respect to gravity on the thermal behaviour of the sample. The experimental results indicate that the unit cell topology is a relevant geometrical parameter which introduces an effect on the thermal performance of the composite which is beyond the mere effect of varying the cell porosity. Indeed, the most porous sample, based on the $f_2$ccz cell type, shows the second lowest wall temperature increase at top heating orientation. The bcc sample shows the highest temperature increase with a 31.2% difference between the two samples. The two samples porosities differ only by 1.2%. At top heating orientation experimental results show a good qualitative agreement with the effective thermal conductivity model proposed by Hubert et al. [23], the transient properties deviate quantitatively from it. Especially, when side and bottom heating configurations are considered, the effect of melt convection on the thermal performance brings to wide variations with respect to the top heating case. Indeed, the bcc sample experiences a 28% wall temperature reduction between the top and bottom heating orientations. This reduces to 21% for the bccz sample, 8% for the $f_2$ccz and 3% for the $f_2$bcc. It is clear that the thermal behaviour of the sample based on the $f_2$bcc unit cell topology, which exhibits the lowest porosity, is dominated by a conductive regime under all heating orientations. To perform a preliminary assessment of the effect of unit cell geometry on the heat transfer, the wall temperature is analysed in relation to the Stefan and Fourier numbers. The strong influence of melt convection on the heat transfer does not allow to obtain a quantifiable correlation. To address the dependency of melt convection on the cell geometry a method to calculate the number of pores and their diameters is implemented and an equivalent pores per inch number is obtained. It is noticed that the tested samples exhibit low number of pores per inch. This suggests that melt convective motion in metallic lattice structures/phase change material composites plays an important role in the definition of the overall heat transfer. Further characterisation of the phenomenon shall allow proper quantification.

As additively manufactured components primarily find application in technological fields where the lightweight is a design driver, it is relevant to address the thermal energy storage potential obtainable by the different samples tested in relation to their porosity and so their overall mass. Thus, a specific thermal performance parameter is introduced. Through this, the $f_2$ccz sample was identified as the best candidate.

The evidence of this work demonstrates that through the variation of unit cell topology in a component, an efficient tailoring of the thermal performance of the composite is achievable. The combined effect of variation of other unit cell geometrical parameters shall be further investigated, also considering the major contribution of melt natural convection. It is to be supposed that a non-trivial optimum can be obtained. Through the flexibility offered by additive manufacturing, local variations to the geometry of a phase change material metallic matrix can be introduced and combined in the same component, leading to locally tailored properties at the unit cell level.

Acknowledgments

We thank Vincenzo Abbatiello from EOS GmbH for the aid in the realization of the samples presented in this work and the software company nTopology® for allowing the use of their tools to support this unfunded research. A special thank goes to Dominik Wagner, and Werner Just whose help was crucial in performing the experiments.

Appendix A

In this appendix, IR frames taken at different times during tests with different inclination are shown for each of the tested cell types.

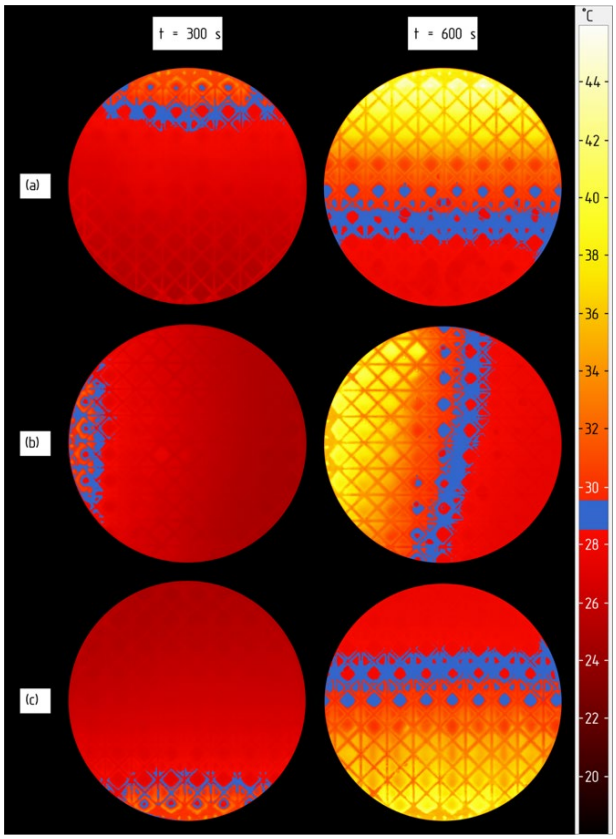

Figure 15:Infrared frame at two different times (t=300s and t=600s) for the three different heating directions for the tests on the **$f_2$ccz** cell type. a) top heating orientation, b) side, c) bottom

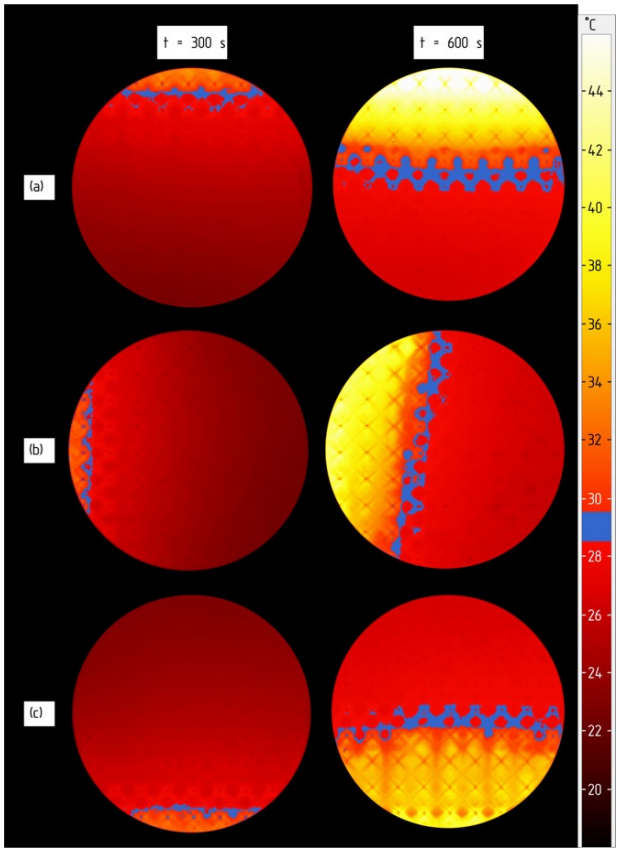

Figure 16: Infrared frame at two different times (t=300s and t=600s) for the three different heating directions for the tests on the **bcc** cell type. a) top heating orientation, b) side, c) bottom

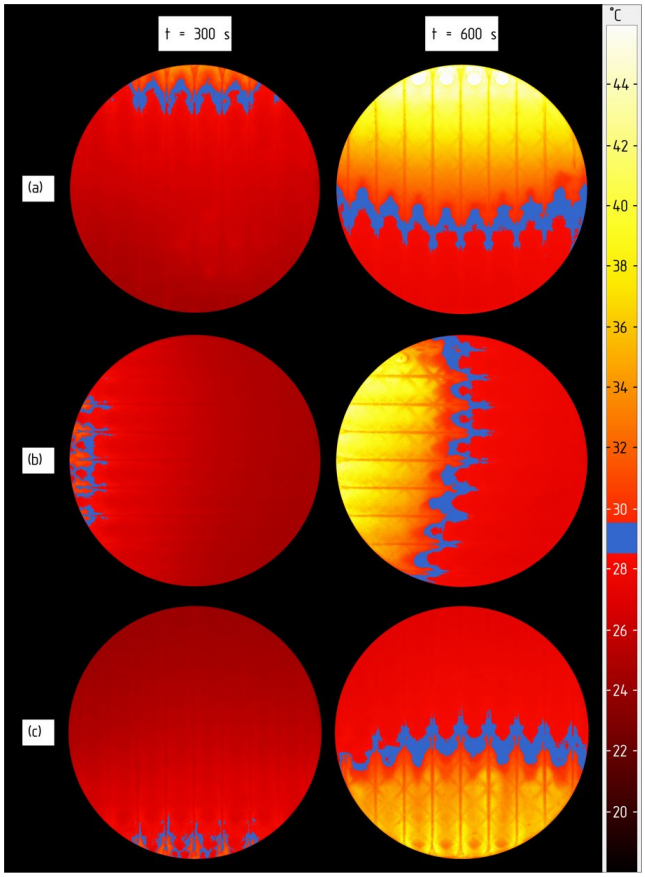

Figure 17: Infrared frame at two different times (t=300s and t=600s) for the three different heating directions for the tests on the **bccz** cell type. a) top heating orientation, b) side, c) bottom

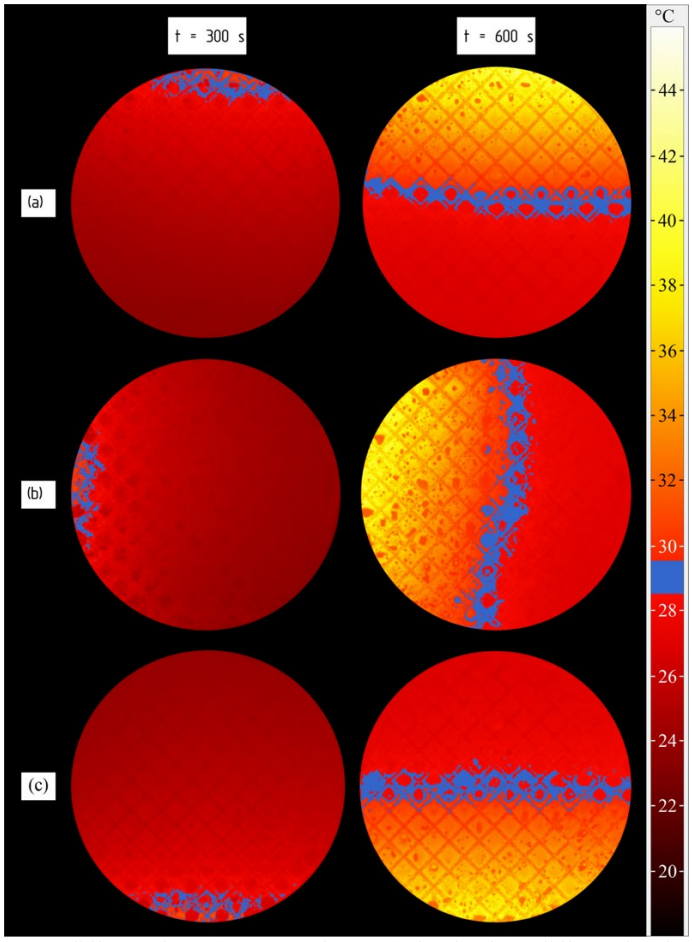

Figure 18: Infrared frame at two different times (t=300s and t=600s) for the three different heating directions for the tests on the **$f_2$bcc** cell type. a) top heating orientation, b) side, c) bottom

Appendix B

Here the temperature evolutions for the remaining bcc, bccz and $f_2$bcc based samples are reported.

bcc

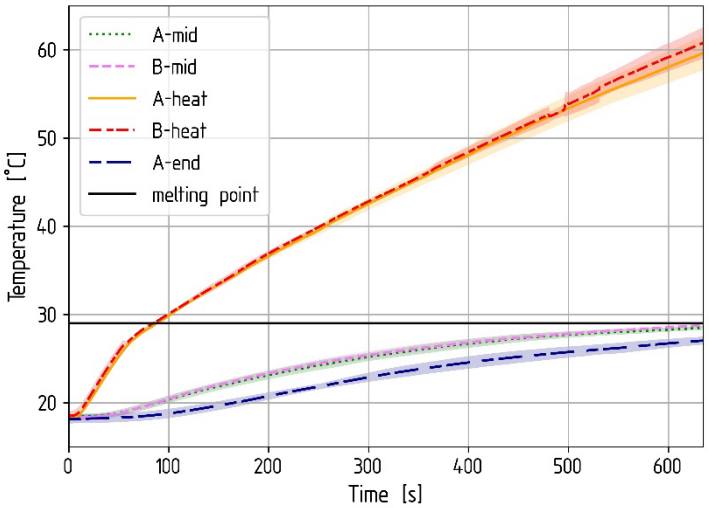

Figure 19: Results of the bcc cell type experiments for the "top" configuration.

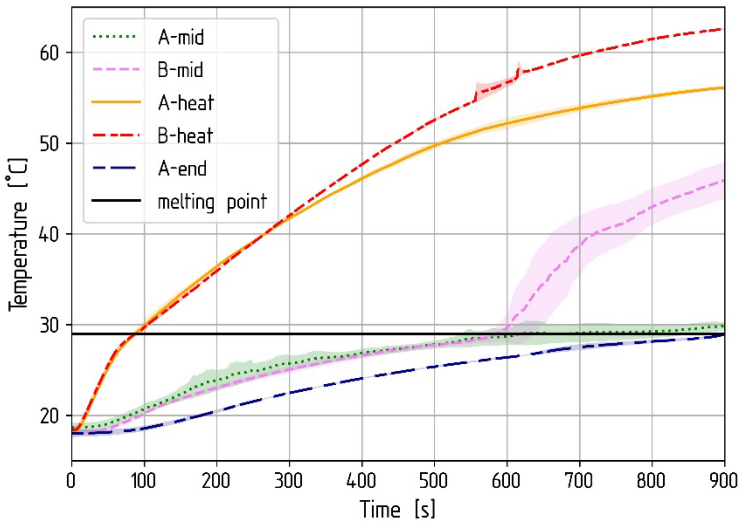

Figure 20: Results of the bcc cell type experiments for the "side" configuration.

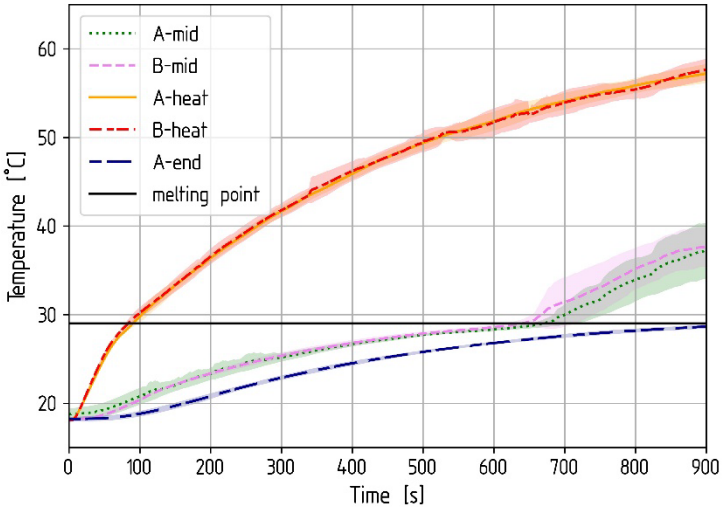

Figure 21: Results of the bcc cell type experiments for the "bottom" configuration.

bccz

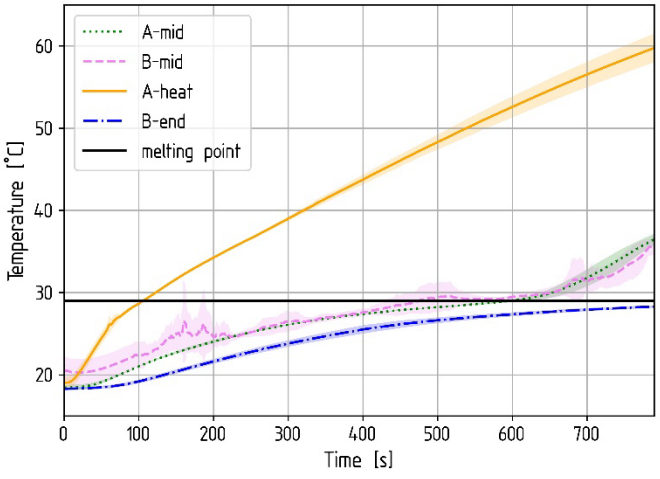

Figure 22: Results of the bccz cell type experiments for the "top" configuration.

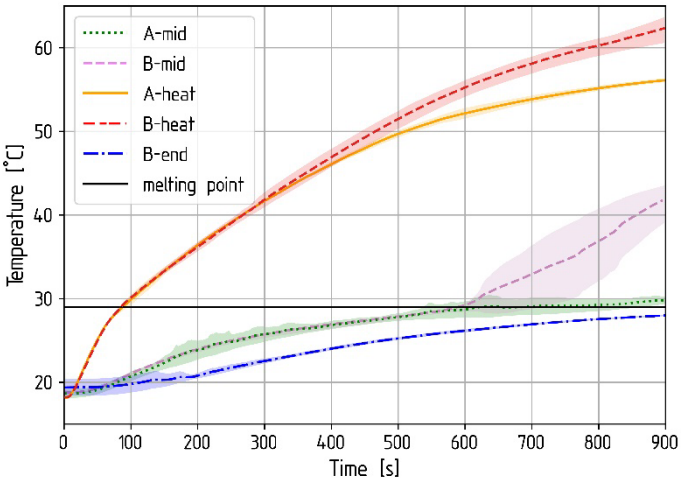

Figure 23: Results of the bccz cell type experiments for the "side" configuration.

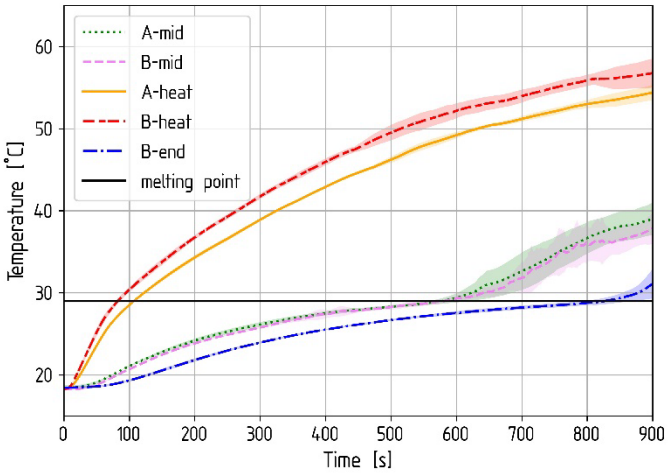

Figure 24: Results of the bccz cell type experiments for the "bottom" configuration.

$f_2$bcc

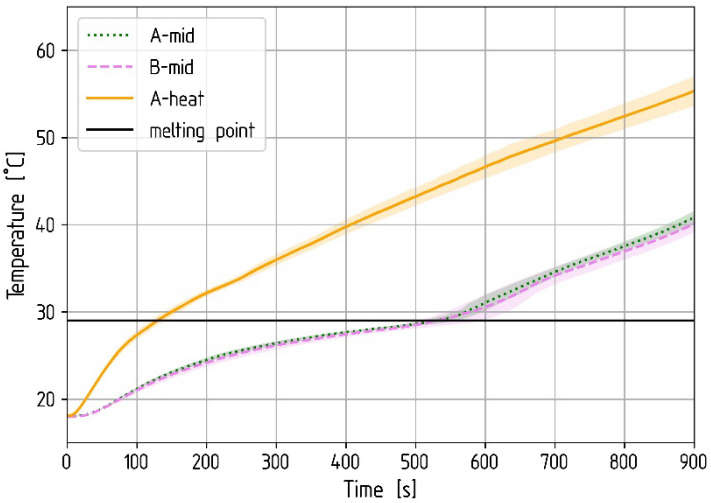

Figure 25: Results of the f2bcc cell type experiments for the "top" configuration.

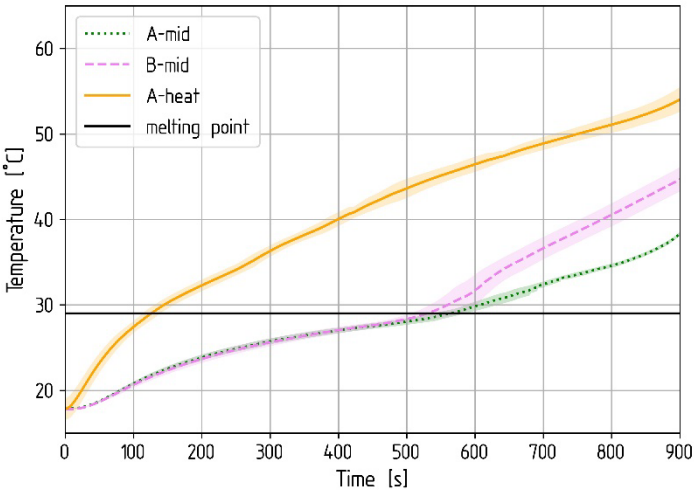

Figure 26: Results of the f2bcc cell type experiments for the "side" configuration.

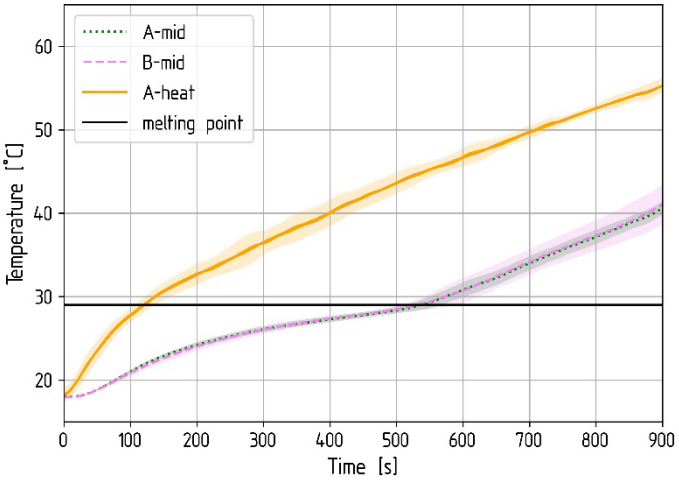

Figure 27: Results of the f2bcc cell type experiments for the "bottom" configuration.

References

[1] K. K. Sairajan, G. S. Aglietti, and K. M. Mani, 'A review of multifunctional structure technology for aerospace applications', *Acta Astronaut.*, vol. 120, pp. 30–42, Mar. 2016, doi: 10.1016/j.actaastro.2015.11.024.

[2] G. Fredi, A. Dorigato, L. Fambri, and A. Pegoretti, 'Multifunctional structural composites for thermal energy storage', *Multifunct. Mater.*, vol. 3, no. 4, p. 042001, Nov. 2020, doi: 10.1088/2399-7532/abc60c.

[3] G. Fredi, A. Dorigato, L. Fambri, S. H. Unterberger, and A. Pegoretti, 'Effect of phase change microcapsules on the thermo-mechanical, fracture and heat storage properties of unidirectional carbon/epoxy laminates', *Polym. Test.*, vol. 91, p. 106747, Nov. 2020, doi: 10.1016/j.polymertesting.2020.106747.

[4] M. Al-Maghalseh and K. Mahkamov, 'Methods of heat transfer intensification in PCM thermal storage systems: Review paper', *Renew. Sustain. Energy Rev.*, vol. 92, pp. 62–94, Sep. 2018, doi: 10.1016/j.rser.2018.04.064.

[5] Tauseef-ur-Rehman, H. M. Ali, M. M. Janjua, U. Sajjad, and W.-M. Yan, 'A critical review

on heat transfer augmentation of phase change materials embedded with porous materials/foams', *Int. J. Heat Mass Transf.*, vol. 135, pp. 649–673, Jun. 2019, doi: 10.1016/j.ijheatmasstransfer.2019.02.001.
[6] S. Filippeschi, M. Mameli, and P. D. Marco, 'EXPERIMENTAL ANALYSIS OF THE MELTING PROCESS IN A PCM/ALUMINUM FOAM COMPOSITE MATERIAL IN HYPERGRAVITY CONDITIONS', *Interfacial Phenom. Heat Transf.*, vol. 6, no. 4, 2018, doi: 10.1615/InterfacPhenomHeatTransfer.2019030703.
[7] C. Ding, C. Zhang, L. Ma, and A. Sharma, 'Numerical investigation on melting behaviour of phase change materials/metal foam composites under hypergravity conditions', *Appl. Therm. Eng.*, vol. 207, p. 118153, May 2022, doi: 10.1016/j.applthermaleng.2022.118153.
[8] M. Iasiello, M. Mameli, S. Filippeschi, and N. Bianco, 'Metal foam/PCM melting evolution analysis: Orientation and morphology effects', *Appl. Therm. Eng.*, vol. 187, p. 116572, Mar. 2021, doi: 10.1016/j.applthermaleng.2021.116572.
[9] G. K. Marri and C. Balaji, 'Experimental and numerical investigations on the effect of porosity and PPI gradients of metal foams on the thermal performance of a composite phase change material heat sink', *Int. J. Heat Mass Transf.*, vol. 164, p. 120454, Jan. 2021, doi: 10.1016/j.ijheatmasstransfer.2020.120454.
[10] A. Parida, A. Bhattacharya, and P. Rath, 'Effect of convection on melting characteristics of phase change material-metal foam composite thermal energy storage system', *J. Energy Storage*, vol. 32, p. 101804, Dec. 2020, doi: 10.1016/j.est.2020.101804.
[11] O. Rehme and C. Emmelmann, 'Rapid manufacturing of lattice structures with selective laser melting', San Jose, CA, Feb. 2006, p. 61070K. doi: 10.1117/12.645848.
[12] L. J. Gibson and M. F. Ashby, *Cellular Solids: Structure and Properties*, 2nd ed. Cambridge University Press, 1997. doi: 10.1017/CBO9781139878326.
[13] M. F. Ashby, 'The properties of foams and lattices', *Philos. Trans. R. Soc. Math. Phys. Eng. Sci.*, vol. 364, no. 1838, pp. 15–30, Jan. 2006, doi: 10.1098/rsta.2005.1678.
[14] N. A. Fleck, V. S. Deshpande, and M. F. Ashby, 'Micro-architectured materials: past, present and future', *Proc. R. Soc. Math. Phys. Eng. Sci.*, vol. 466, no. 2121, pp. 2495–2516, Sep. 2010, doi: 10.1098/rspa.2010.0215.
[15] H. Wadley, 'Fabrication and structural performance of periodic cellular metal sandwich structures', *Compos. Sci. Technol.*, vol. 63, no. 16, pp. 2331–2343, Dec. 2003, doi: 10.1016/S0266-3538(03)00266-5.
[16] H. N. G. Wadley, 'Multifunctional periodic cellular metals', *Philos. Trans. R. Soc. Math. Phys. Eng. Sci.*, vol. 364, no. 1838, pp. 31–68, Jan. 2006, doi: 10.1098/rsta.2005.1697.
[17] N. Wicks and J. W. Hutchinson, 'Optimal truss plates', *Int. J. Solids Struct.*, vol. 38, no. 30–31, pp. 5165–5183, Jul. 2001, doi: 10.1016/S0020-7683(00)00315-2.
[18] Y. Shen, S. Mckown, S. Tsopanos, C. J. Sutcliffe, R. A. W. Mines, and W. J. Cantwell, 'The Mechanical Properties of Sandwich Structures Based on Metal Lattice Architectures', *J. Sandw. Struct. Mater.*, vol. 12, no. 2, pp. 159–180, Mar. 2010, doi: 10.1177/1099636209104536.
[19] R. Mines, *Metallic Microlattice Structures: Manufacture, Materials and Application*. Cham: Springer International Publishing, 2019. doi: 10.1007/978-3-030-15232-1.
[20] Y. Zhang, G. Ma, J. Wang, S. Liu, and S. Kang, 'Numerical and experimental study of phase-change temperature controller containing graded cellular material fabricated by additive manufacturing', *Appl. Therm. Eng.*, vol. 150, pp. 1297–1305, Mar. 2019, doi: 10.1016/j.applthermaleng.2019.01.066.
[21] G. Righetti, G. Savio, R. Meneghello, L. Doretti, and S. Mancin, 'Experimental study of phase change material (PCM) embedded in 3D periodic structures realized via additive manufacturing', *Int. J. Therm. Sci.*, vol. 153, p. 106376, Jul. 2020, doi: 10.1016/j.ijthermalsci.2020.106376.
[22] J. P. Dudon *et al.*, 'Optimized Phase Change Material Module for Thermal Regulation of Cycled Dissipative Units', Jul. 2019.
[23] R. Hubert *et al.*, 'An effective thermal conductivity model for architected phase change material enhancer: Theoretical and experimental investigations', *Int. J. Heat Mass Transf.*, vol. 176, p. 121364, Sep. 2021, doi: 10.1016/j.ijheatmasstransfer.2021.121364.
[24] A. Diani and M. Campanale, 'Transient melting of paraffin waxes embedded in aluminum

foams: Experimental results and modeling', *Int. J. Therm. Sci.*, vol. 144, pp. 119–128, Oct. 2019, doi: 10.1016/j.ijthermalsci.2019.06.004.
[25] D. Groulx and M. Lacroix, 'Study of close contact melting of ice from a sliding heated flat plate', *Int. J. Heat Mass Transf.*, vol. 49, no. 23–24, pp. 4407–4416, Nov. 2006, doi: 10.1016/j.ijheatmasstransfer.2006.05.007.